

Task-Oriented Co-Design of Communication, Computing, and Control for Edge-Enabled Industrial Cyber-Physical Systems

Yufeng Diao, *Graduate Student Member, IEEE*, Yichi Zhang, *Graduate Student Member, IEEE*,
Daniele De Martini, *Member, IEEE*, Philip Guodong Zhao, *Senior Member, IEEE*,
and Emma Liying Li, *Member, IEEE*

Abstract—This paper proposes a task-oriented co-design framework that integrates communication, computing, and control to address the key challenges of bandwidth limitations, noise interference, and latency in mission-critical industrial Cyber-Physical Systems (CPS). To improve communication efficiency and robustness, we design a task-oriented Joint Source-Channel Coding (JSCC) using Information Bottleneck (IB) to enhance data transmission efficiency by prioritizing task-specific information. To mitigate the perceived End-to-End (E2E) delays, we develop a Delay-Aware Trajectory-Guided Control Prediction (DTCP) strategy that integrates trajectory planning with control prediction, predicting commands based on E2E delay. Moreover, the DTCP is co-designed with task-oriented JSCC, focusing on transmitting task-specific information for timely and reliable autonomous driving. Experimental results in the CARLA simulator demonstrate that, under an E2E delay of 1 second (20 time slots), the proposed framework achieves a driving score of 48.12, which is 31.59 points higher than using Better Portable Graphics (BPG) while reducing bandwidth usage by 99.19%.

Index Terms—Task-oriented communication, task-oriented co-design, edge inference, information bottleneck, variational inference.

I. INTRODUCTION

In industrial Cyber-Physical Systems (CPS), ensuring Ultra-Reliable Low-Latency Communications (URLLCs) is crucial for achieving reliable real-time performance [1]. Applications such as automated transportation, material handling, and inspection increasingly rely on autonomous vehicles and robots within factories, warehouses, and hazardous environments. Autonomous driving plays an important role in these systems, enabling the automation of essential tasks, optimizing workflow efficiency, and improving safety [2].

To meet the stringent requirements of URLLC (e.g., the End-to-End (E2E) delay should be less than 1 ms and the

Yufeng Diao is with the School of Computing Science, University of Glasgow, U.K., and is currently a visiting Ph.D. student with the Department of Computer Science, University of Manchester, U.K. (e-mail: y.diao.1@research.gla.ac.uk).

Yichi Zhang is with the Department of Computer Science, University of Manchester, U.K. Part of this work was done when he was with the James Watt School of Engineering, University of Glasgow, U.K. (e-mail: yichi.zhang@postgrad.manchester.ac.uk).

Daniele De Martini is with the Oxford Robotics Institute, Department of Engineering Science, University of Oxford, U.K. (e-mail: daniele@robots.ox.ac.uk).

Philip Guodong Zhao is with the Department of Computer Science, University of Manchester, U.K. (e-mail: philip.zhao@manchester.ac.uk).

Emma Liying Li is with the School of Computing Science, University of Glasgow, U.K. (e-mail: liying.li@glasgow.ac.uk).

packet loss probability should be less than 10^{-5} [3]), edge inference has emerged as a promising solution [4]. By minimizing the physical distance between data generation and processing, edge inference significantly reduces latency, which is vital for autonomous systems that must respond timely to dynamic environmental changes, such as navigating unpredictable factory layouts or reacting to sudden obstacles. The primary motivation for using edge computing (also called off-board computing) lies in its ability to enhance system flexibility, particularly given the differing innovation cycles of the automotive and semiconductor industries. While a vehicle's lifespan typically ranges from 10 to 20 years, advancements in computing capabilities can be significant within this period. By leveraging edge computing within shared telecommunication infrastructure, the vehicle can enjoy much better flexibility in upgrading the computing power and software throughout their entire lifetime. However, the transmission of massive amounts of sensor and video data presents a challenge to the edge's ability to handle real-time processing while maintaining the reliability and low-latency communications. In that case, edge inference, often powered by Deep Neural Networks (DNNs), is still affected by nontrivial communication latency and bandwidth constraints, particularly under the demands of URLLC in industrial CPS [5].

Recent developments in deep learning have introduced Joint Source-Channel Coding (JSCC) as a promising solution to the limited communication bandwidth and significant noise interference [6]. Unlike traditional separate coding designs, JSCC integrates source and channel coding, improving data transmission efficiency. Despite these advantages, conventional JSCC approaches typically focus on accurate signal reconstruction at the receiver, potentially wasting communication resources on task-agnostic information that does not directly contribute to the decision-making process [7]. This inefficiency has attracted significant research interest in task-oriented communication, a technology designed to prioritize the transmission of task-specific information, thus reducing data rates and improving efficiency, especially for AI-driven applications [8].

Furthermore, data sent to the edge server become outdated due to uplink delays, including processing, transmission, propagation, and queueing delay, negatively impacting the timeliness of edge inference results. This issue is further exacerbated by downlink, computing, and control delays. The E2E delay (round-trip delay) degrades system performance and makes

it difficult to meet the URLLC requirements in industrial CPS. Prediction-based methods can mitigate perceived E2E delay [9], but longer prediction horizons increase the risk of inaccuracy, creating a trade-off between minimizing delay and ensuring reliability.

Given the limitations of traditional approaches that design communication, computing, and control components separately, an integrated task-oriented co-design framework becomes essential [10]–[12]. In this work, our objective is to address three fundamental questions for edge-enabled mission-critical industrial CPS: 1) How can data transmission be optimized for bandwidth-constrained and latency-sensitive applications to ensure that task-specific information is prioritized? 2) How can predictive models be utilized to ensure that edge inference systems make decisions that reduce perceived E2E delay? 3) How can communication, computing, and control be jointly designed and optimized to meet the demands of URLLC in mission-critical applications? The key contributions of this paper are summarized as follows:

- We develop a comprehensive task-oriented co-design framework that jointly optimizes communication, computing, and control. This framework seamlessly integrates task-oriented JSCC with a delay-aware autonomous driving agent, addressing the critical challenges of bandwidth constraints, noise interference, and E2E delay to maximize performance for edge-enabled autonomous driving.
- We formulate the problem of task-oriented communication using the Information Bottleneck (IB) approach and employ a variational approximation to derive a tractable upper bound, resulting in the Variational Information Bottleneck (VIB) method. Additionally, we extend the standard VIB framework to incorporate conditional information, such as vehicle and channel state information, ensuring better alignment with mission-critical applications. Furthermore, we handle the KL-divergence term using a concise approach inspired by [13]. Our formulation improves communication efficiency in dynamic and noisy environments, which is essential for the reliable operation of industrial CPS.
- We establish the Delay-aware Trajectory-guided Control Prediction (DTCP) strategy for autonomous driving, which uniquely combines two dominant autonomous driving paradigms: trajectory planning and control prediction. The DTCP processes JSCC symbols, state information, and channel state to predict optimal driving actions that reduce perceived E2E delay. In addition, DTCP is specially co-designed with the task-oriented JSCC and is jointly trained for machine-to-machine communication.

The rest of this paper is organized as follows. The related works are presented in Section II. In Section III, we introduce the system model and formulate the variational problem. Section V presents the details of DTCP and the proposed co-design with task-oriented JSCC. The numerical and experimental results are provided in Section VI. Finally, conclusions are drawn in Section VII.

The main notations used throughout the paper are summarized in Table I. To improve readability and manage the

complexity of the joint design of communication, computation, and control, the temporal subscript of the notation is omitted in Section III.

II. RELATED WORKS

a) Task-oriented Joint Source-Channel Coding: The integration of deep learning into communication systems has introduced groundbreaking possibilities that go beyond conventional boundaries [14]. Unlike traditional methods that separate source and channel coding, deep JSCC offers an end-to-end learning-based approach, optimizing the information transmission holistically. Previous research has highlighted the superiority of deep JSCC for reconstruction-oriented communication [6], [7], [15] over traditional source coding (e.g., JPEG [16] and JPEG2000 [17]) and channel coding (e.g., LDPC codes [18]) methods, especially in low-Signal-to-Noise Ratio (SNR) environments.

However, most reconstruction-oriented approaches have focused primarily on data-centric metrics, often leading to suboptimal task performance. High-fidelity reconstructions are not always necessary for machine-to-machine communication, whereas preserving task-specific information is more important [8], [19]–[24]. Driven by the growing demand for task-oriented communication designs, researchers have increasingly explored the IB approach. The IB [25] method seeks to maximize the preservation of task-specific information while minimizing task-agnostic information from input. Traditional IB approach relied on the computationally intensive Blahut-Arimoto algorithm [26], [27], which was impractical for deep learning applications due to its complexity [28]. This limitation was addressed by the introduction of a variational approach to the IB method, known as VIB [29], which made it feasible to apply IB principles in deep learning by approximating the true posterior with a variational distribution.

Recent studies have successfully integrated VIB with deep JSCC, formalizing task-oriented communication strategies that outperform traditional reconstruction-oriented frameworks. For example, recent works [12], [30] have demonstrated that combining VIB with deep JSCC can significantly improve communication efficiency and robustness, particularly in scenarios where it is essential to prioritize task-specific information over the fidelity of raw data. Another study [31] focused on applying semantic communication for camera relocalization, optimizing the trade-off between inference accuracy and E2E latency.

b) Edge Inference: To meet the stringent latency demands of modern applications, edge inference has emerged as a crucial solution that effectively addresses the limitations of traditional cloud-based architectures [32], [33]. A key innovation in this domain is the *split inference*, where the inference process is divided between the edge device and the server. In split inference architectures, a lightweight neural network on the mobile device extracts compact feature vectors from the data, which are then transmitted to an edge server for further analysis. This architecture allows for initial data processing on the device, followed by more intensive computations at the edge, thus reducing latency and improving overall system

TABLE I
SUMMARY OF MAIN SYMBOLS

\mathbf{x}	Input image (data)	K_b	Size of mini-batch
X	Random variable of \mathbf{x}	\mathbf{x}_t	Image captured by a camera at time t
\mathcal{X}	Space of \mathbf{x}	$\mathbf{z}_t^{l(t)}, \mathbf{z}_t^l$	JSCC symbols with length l transmitted at time t
\mathbf{z}	Transmitted JSCC symbols	$\hat{\mathbf{z}}_{t-\delta_{eu}}^{l(t-\delta_{eu})}, \hat{\mathbf{z}}_{t-\delta_{eu}}^l$	Reconstructed JSCC symbols with length l received at time t
Z	Random variable of \mathbf{z}	\mathbf{m}_t	State information transmitted at time t
$\hat{\mathbf{z}}$	Reconstructed JSCC symbols	τ	Duration of time slot
\mathcal{Z}	Space of JSCC symbols	D_t	Index set for \mathbf{z}_t^l
$\tilde{\mathbf{z}}$	Received JSCC symbols	δ_e	Computing delay of JSCC encoding
h	Channel state	δ_u	Uplink communication delay
\mathbf{n}	Gaussian noise	δ_a	Computing delay of agent
H	Random variable of h	δ_d	Downlink communication delay
\mathcal{H}	Space of h	δ_c	Control delay
\mathbf{m}	State information	δ_{eu}	Combined delay of δ_e and δ_u
M	Random variable of \mathbf{m}	δ	End-to-end delay
\mathcal{M}	Space of \mathbf{m}	δ_T	Delay threshold
\mathbf{a}	Ground-truth action	l_p	Prediction horizon
A	Random variable of \mathbf{a}	l_w	Extra Prediction Horizon
$\hat{\mathbf{a}}$	Estimated action	$\mathbf{r}_{t-\delta_{eu}}^{\text{traj}}$	Trajectory feature corresponding to $x_{t-\delta_{eu}}$
\hat{A}	Random variable of $\hat{\mathbf{a}}$	$\mathcal{R}_{\text{traj}}$	Space of trajectory features
\mathcal{A}	Space of action	$\mathbf{h}_{t-\delta_{eu}}^{\text{traj}}$	Trajectory hidden state corresponding to $x_{t-\delta_{eu}}$
$f_e(\cdot)$	Function of JSCC encoder	$\mathbf{w}_{t-\delta_{eu}}$	Planned waypoint at time $t - \delta_{eu}$
$f_h(\cdot)$	Function of noisy fading channel	$\mathbf{c}_{t-\delta_{eu}+l_p}^{\text{traj}}$	Predicted trajectory command with horizon l_p for $x_{t-\delta_{eu}}$
$f_a(\cdot)$	Function of autonomous driving agent	$\mathbf{r}_{t-\delta_{eu}}^{\text{ctrl}}$	Control feature corresponding to $x_{t-\delta_{eu}}$
P_{target}	Average power constraint of \mathbf{z}	$\mathcal{R}_{\text{ctrl}}$	Space of control features
l_x	Dimension of \mathbf{x}	$\mathbf{h}_{t-\delta_{eu}}^{\text{ctrl}}$	Control hidden state corresponding to $x_{t-\delta_{eu}}$
l_z	Dimension of \mathbf{z}	$\mathbf{c}_{t-\delta_{eu}+l_p}^{\text{ctrl}}$	Predicted control command with horizon l_p for $x_{t-\delta_{eu}}$
$g(\cdot, \cdot)$	Distortion measuring function	$\mathbf{c}_{t-\delta_{eu}+l_p}^{\text{comb}}$	Predicted combined command with horizon l_p for $x_{t-\delta_{eu}}$
ζ_{ratio}	Constraint of bandwidth compression ratio	\mathcal{C}_{cmd}	Space of commands
ζ_{rate}	Constraint of rate	$f_{\text{feat-t}}(\cdot, \cdot, \cdot)$	Function of trajectory feature extractor
ϕ	Parameters of JSCC encoder	$f_{\text{traj}}(\cdot)$	Function of trajectory branch
ψ	Parameters of autonomous driving agent	$f_{\text{feat-c}}(\cdot, \cdot, \cdot)$	Function of control feature extractor
β	Lagrange multiplier	$f_{\text{ctrl}}(\cdot, \cdot)$	Function of control branch
$f_{\mu}(\cdot)$	Function for estimating the mean of reconstructed JSCC symbols	$f_{\text{comb}}(\cdot, \cdot)$	Function of command combination
$f_{\sigma}(\cdot)$	Function for estimating the standard deviation of reconstructed JSCC symbols	$\lambda_c, \lambda_{\text{feat}}, \lambda_{\text{value}}, \lambda_{\text{speed}}, \lambda_{\text{traj}}, \lambda_{\text{ctrl}}, \lambda_{\text{aux}}$	Hyperparameters of agent
K_a	Size of dataset	i	General index depended on the context

efficiency [34]–[40]. Deep JSCC plays a critical role in this process by enabling efficient compression and transmission of these intermediate features [12], [30], [37]–[40].

Recent studies [12], [30], [38], [41], [42] have increasingly focused on inference accuracy as a key performance indicator, highlighting the shift in communication systems towards optimizing task-specific performance rather than data-centric metrics. In particular, [12] introduced a method that dynamically adjusts the length of the transmitted signal in response to varying communication conditions, ensuring that required inference accuracy is maintained while optimizing the use of available resources.

c) Predictions in URLLC Applications: In the context of URLLC, prediction-based methods have been explored to mitigate delays. For instance, [43] proposed a technique to predict movements or force feedback to reduce perceived delay in Tactile Internet applications. Similarly, [44] presented a co-design approach for packetized predictive control (PPC) in real-time CPS, addressing the delay in the tight interaction between wireless communication and control systems. For visual content, [45] investigated how predictive displays can mitigate communication delays in telesurgery using Augmented Reality (AR) technology. The proposed system provided real-time visual feedback to surgeons by

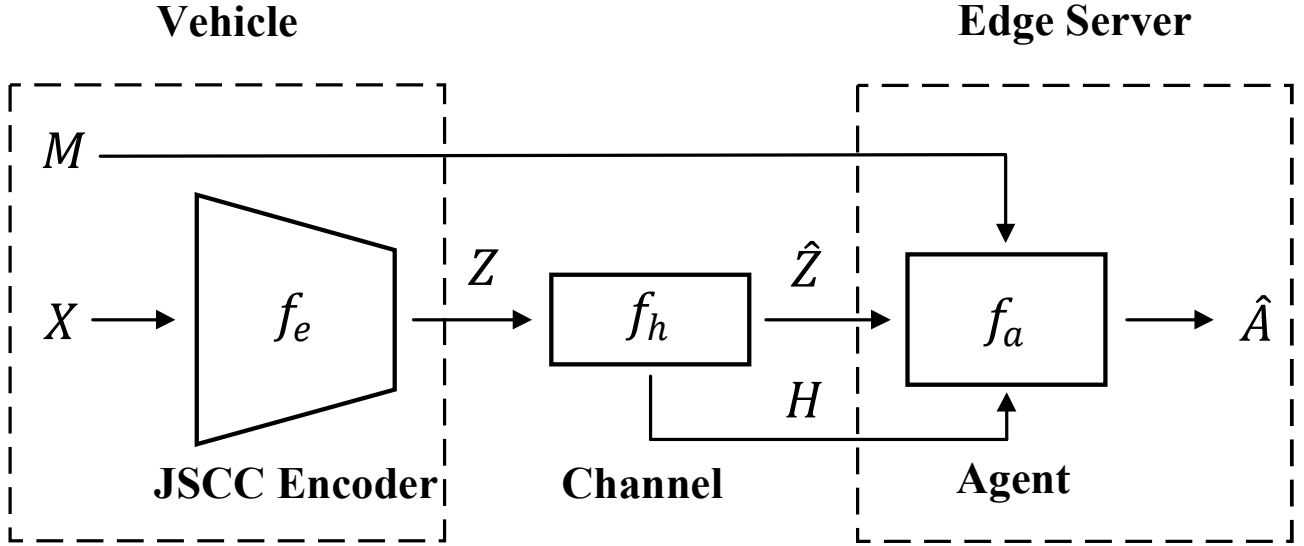


Fig. 1. General framework of edge-enabled autonomous driving.

predicting movements of robotic tools, significantly improving task completion times under latency without increasing error rates. Likewise, [46] introduced edge intelligence to predict user motion, enabling pre-rendering and caching of Virtual Reality (VR) content, thus significantly reducing the latency in VR streaming. However, in these studies [43]–[46], the trade-off between the prediction horizon and the reliability of the system was not adequately addressed. To bridge this gap, [9] focused on the challenges of delay and reliability in URLLC by co-designing prediction and communication systems. The proposed framework enables mobile devices to predict future states and send these predictions to a data center in advance, thus reducing perceived delays. The study also analyzed the trade-off between prediction accuracy and system reliability, demonstrating that longer prediction horizons increase the likelihood of errors.

III. SYSTEM MODEL AND PROBLEM FORMULATION

As shown in Fig. 1, we consider an edge server that provides computing service for a single vehicle (device). The vehicle transmits JSCC symbols and encoded state information to the edge server. After processing the received data, the edge server sends the drive commands back to the vehicle.

The on-vehicle JSCC encoder f_e is defined as:

$$f_e : \mathcal{X} \rightarrow \mathcal{Z} : \mathbf{x} \mapsto \mathbf{z}, \quad (1)$$

where $\mathbf{x} \in \mathbb{R}^{l_x}$ denotes the input image, and $\mathbf{z} = [z_1, \dots, z_{l_z}] \in \mathbb{C}^{l_z}$ denotes the transmitted JSCC symbols. Here, l_x denotes the source bandwidth, which is the product of the height, width, and number of color channels of the image \mathbf{x} . The parameter l_z denotes the channel bandwidth. We define l_z/l_x as the *bandwidth compression ratio* [6]. In particular, the transmitted JSCC symbols should satisfy the

average power constraint P_{target} :

$$\frac{1}{l_z} \sum_{i=1}^{l_z} |z_i|^2 \leq P_{\text{target}}. \quad (2)$$

Then \mathbf{z} are transmitted to the edge server via communication channels, which can be mathematically represented by the function:

$$f_h : \mathcal{Z} \rightarrow \mathcal{Z} : \mathbf{z} \mapsto \hat{\mathbf{z}}. \quad (3)$$

In this paper, we model the communication channel as a frequency-selective channel implemented through Orthogonal Frequency-Division Multiplexing (OFDM) to mitigate multipath fading, as detailed in [47]:

$$\tilde{\mathbf{z}} = f_h(\mathbf{z}) = \mathbf{h} \cdot \mathbf{z} + \mathbf{n}, \quad (4)$$

where $\tilde{\mathbf{z}}$ denotes the received JSCC symbols, and $\mathbf{n} \sim \mathcal{CN}(0, \sigma_n^2 \mathbf{I})$ represents complex Gaussian noise with zero mean and standard deviation σ_n , where \mathbf{I} denotes the identity matrix and σ_n is a diagonal matrix. The channel frequency response $\mathbf{h} \in \mathbb{C}^{l_z}$ captures the characteristics of multipath fading. A comprehensive modeling of the OFDM channel is provided in Appendix A.

In this paper, we assume the perfect Channel State Information (CSI). After receiving, the JSCC symbols are equalized:

$$\hat{\mathbf{z}} = \frac{h^*}{|h|^2} \tilde{\mathbf{z}}, \quad (5)$$

where h^* denotes the conjugate of channel coefficient h and $\hat{\mathbf{z}}$ denotes the reconstructed JSCC symbols.

Following transmission, the reconstructed JSCC symbols $\hat{\mathbf{z}}$ are processed by the autonomous driving agent f_a with state information and channel state, which is defined as:

$$f_a : \mathcal{Z} \times \mathcal{M} \times \mathcal{H} \rightarrow \mathcal{A} : (\hat{\mathbf{z}}, \mathbf{m}, \mathbf{h}) \mapsto \hat{\mathbf{a}}, \quad (6)$$

where $\hat{\mathbf{a}} \sim p(\hat{\mathbf{a}})$ denotes the estimated action, which approximates the ground-truth action $\mathbf{a} \sim p(\mathbf{a})$. In addition, \mathbf{m}

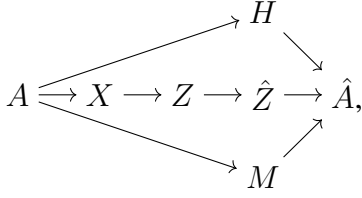


Fig. 2. The DPGM for edge-enabled autonomous driving.

denotes state information consisting of vehicle speed, discrete navigation command, destination coordinates, and timestamp. The agent incorporates vehicle state information \mathbf{m} and channel state information \mathbf{h} as conditional inputs, establishing a direct link between communication and control to improve decision-making. Since the state information \mathbf{m} typically consumes negligible bandwidth (in this work, \mathbf{m} consists of four floating-point numbers and one integer), we assume that it is received losslessly by the edge server, provided that the corresponding image is successfully received and decoded.

The task-oriented objective of edge-enabled autonomous driving is to minimize the expected distortion between the ground-truth action \mathbf{a} and the estimated action $\hat{\mathbf{a}}$, which is defined as $g : \mathcal{A} \times \mathcal{A} \rightarrow \mathbb{R}^+$. Consequently, the problem of the proposed task-oriented co-design is defined in Problem 1.

Problem 1.

$$\min_{f_e, f_a} \mathbb{E}_{\mathbf{a} \sim p(\mathbf{a}|\hat{\mathbf{z}}, \mathbf{m}, \mathbf{h})} \left\{ \mathbb{E}_{\hat{\mathbf{a}} \sim p(\hat{\mathbf{a}}|\hat{\mathbf{z}}, \mathbf{m}, \mathbf{h})} [g(\mathbf{a}, \hat{\mathbf{a}})] \right\} \quad (7)$$

$$\text{s.t. } l_z/l_x - \zeta_{\text{ratio}} \leq 0, \quad (8)$$

$$(1), (2), (3), (4), (6), \quad (9)$$

where ζ_{ratio} denotes an upper bound of the bandwidth compression ratio.

Problem 1 is an abstract formulation that describes the overarching goal of optimizing task performance through appropriate parameter selection. However, directly solving Problem 1 poses significant computational challenges, particularly in the evaluation of the expectation over random variables, which involves integration that can be computationally prohibitive. In addition, finding a proper objective function $g(\cdot, \cdot)$ is also difficult. In the following section, we introduce the VIB approach combined with DNNs to effectively address Problem 1.

IV. VARIATIONAL INFORMATION BOTTLENECK APPROACH

Based on the discussion in Section III, the Directed Probabilistic Graphical Model (DPGM) of the proposed framework can be depicted as shown in Fig. 2, where A , X , Z , \hat{Z} , M , H and \hat{A} denotes the random variables of the ground-truth action \mathbf{a} , input images \mathbf{x} , transmitted JSCC symbols \mathbf{z} , reconstructed JSCC symbols $\hat{\mathbf{z}}$, state information \mathbf{m} , channel state \mathbf{h} , and estimated action $\hat{\mathbf{a}}$, respectively. With this DPGM, the IB can be formulated as an optimization problem:

$$\begin{aligned} \min_{\phi, \psi} & -I(A; \hat{Z}, M, H) \\ \text{s.t.} & I(X; \hat{Z}) - \zeta_{\text{rate}} \leq 0, \end{aligned} \quad (10)$$

where ϕ and ψ are the parameters of JSCC encoder f_e and autonomous driving agent f_a , respectively. ζ_{rate} denotes the upper bound of the rate. Eq. (10) is derived as a practical and task-oriented reformulation of Problem 1. The objective function in Eq. (10), $I(A; \hat{Z}, M, H)$, measures the information shared between the target variable A and the combined set of variables (\hat{Z}, M, H) . By minimizing $-I(A; \hat{Z}, M, H)$, we ensure that the information about A retained in (\hat{Z}, M, H) is maximized, aligning the optimization with the task-specific objectives of Problem 1. This is supported by the DPGM structure where \hat{A} depends on (\hat{Z}, M, H) , highlighting that preserving information about A in these variables is key to achieving optimal task performance. Moreover, the constraints in Eq. (10) explicitly incorporate communication limitations through the term $I(X, \hat{Z})$, which limits the rate of transmitted information. These constraints parallel the bandwidth restrictions in Problem 1, thereby ensuring consistency between the two formulations.

By introducing the Lagrange multiplier β , IB can be further formulated to minimize the following objective function:

$$\mathcal{L}_{\text{IB}} := \underbrace{-I(A; \hat{Z}, M, H)}_{\text{Distortion}} + \beta \underbrace{I(X; \hat{Z})}_{\text{Rate}}. \quad (11)$$

Building on the foundational works of [12] and [29], we develop a VIB approach to approximate each term in Eq. (11), addressing the intractability of mutual information. The first term $-I(A; \hat{Z}, M, H)$ can be expressed as:

$$\begin{aligned} & -I(A; \hat{Z}, M, H) \\ &= - \int p(\mathbf{a}, \hat{\mathbf{z}}, \mathbf{m}, \mathbf{h}) \log \frac{p(\mathbf{a}|\hat{\mathbf{z}}, \mathbf{m}, \mathbf{h})}{p(\mathbf{a})} d\mathbf{a} d\hat{\mathbf{z}} d\mathbf{m} d\mathbf{h} \\ &= - \int p(\mathbf{a}, \hat{\mathbf{z}}, \mathbf{m}, \mathbf{h}) \log p(\mathbf{a}|\hat{\mathbf{z}}, \mathbf{m}, \mathbf{h}) d\mathbf{a} d\hat{\mathbf{z}} d\mathbf{m} d\mathbf{h} \\ & \quad - H(A), \end{aligned} \quad (12)$$

where $H(A)$ denotes the entropy of random variable A , which is independent of the optimization and thus can be ignored. In addition, $p(\mathbf{a}|\hat{\mathbf{z}}, \mathbf{m}, \mathbf{h})$ is the posterior probability, which can be derived from the DPGM [12], [29] as:

$$\begin{aligned} p(\mathbf{a}|\hat{\mathbf{z}}, \mathbf{m}, \mathbf{h}) &= \int p(\mathbf{a}, \mathbf{x}, \mathbf{z}|\hat{\mathbf{z}}, \mathbf{m}, \mathbf{h}) d\mathbf{x} d\mathbf{z} \\ &= \int \frac{p(\mathbf{a})p(\mathbf{x}|\mathbf{a})p_\phi(\mathbf{z}|\mathbf{x})p(\hat{\mathbf{z}}|\mathbf{z})p(\mathbf{m}|\mathbf{a})p(\mathbf{h}|\mathbf{a})}{p(\hat{\mathbf{z}}, \mathbf{m}, \mathbf{h})} d\mathbf{x} d\mathbf{z}. \end{aligned} \quad (13)$$

Since this integration is intractable in our case, we use $q_\psi(\mathbf{a}|\hat{\mathbf{z}}, \mathbf{m}, \mathbf{h})$ as a variational approximation of $p(\mathbf{a}|\hat{\mathbf{z}}, \mathbf{m}, \mathbf{h})$. Based on the fact that Kullback-Leibler (KL) divergence is always non-negative, the following inequality can be obtained:

$$\begin{aligned} & -I(A; \hat{Z}, M, H) + H(A) \\ &= \mathbb{E}_{\mathbf{a}, \mathbf{x}} \left[\mathbb{E}_{\hat{\mathbf{z}}|\mathbf{x}; \phi} \left[\mathbb{E}_{\mathbf{m}, \mathbf{h}} [-\log p(\mathbf{a}|\hat{\mathbf{z}}, \mathbf{m}, \mathbf{h})] \right] \right] \\ &\leq \mathbb{E}_{\mathbf{a}, \mathbf{x}} \left[\mathbb{E}_{\hat{\mathbf{z}}|\mathbf{x}; \phi} \left[\mathbb{E}_{\mathbf{m}, \mathbf{h}} [-\log q_\psi(\mathbf{a}|\hat{\mathbf{z}}, \mathbf{m}, \mathbf{h})] \right] \right]. \end{aligned} \quad (14)$$

The second term $I(X; \hat{Z})$ can be formulated as:

$$I(X; \hat{Z}) = \mathbb{E}_{\mathbf{a}, \mathbf{x}} [D_{\text{KL}}(p_\phi(\hat{\mathbf{z}}|\mathbf{x})||p(\hat{\mathbf{z}}))], \quad (15)$$

where $p(\hat{\mathbf{z}})$ is the intractable prior probability of $\hat{\mathbf{z}}$. Instead of using approximation proposed in [48], we adopt a predefined Gaussian distribution $q(\hat{\mathbf{z}}) \sim \mathcal{N}(\boldsymbol{\mu}_{\hat{\mathbf{z}}}, \boldsymbol{\sigma}_{\hat{\mathbf{z}}}^2 I)$ as the approximation of $p(\hat{\mathbf{z}})$ [13], where $\boldsymbol{\mu}_{\hat{\mathbf{z}}}$ and $\boldsymbol{\sigma}_{\hat{\mathbf{z}}}$ represent the mean and standard deviation of the Gaussian distribution, respectively.

In addition, we model the JSCC encoder f_e as a probability model $p_\phi(\mathbf{z}|\mathbf{x})$. Considering that $p_\phi(\hat{\mathbf{z}}|\mathbf{x}) = \int p_\phi(\mathbf{z}|\mathbf{x})p(\hat{\mathbf{z}}|\mathbf{z})d\mathbf{z}$, where $p(\hat{\mathbf{z}}|\mathbf{z})$ represents the probabilistic nature of the channel function f_h , and assuming perfect CSI, we define $p_\phi(\hat{\mathbf{z}}|\mathbf{x}) \sim \mathcal{N}(f_\mu(\hat{\mathbf{z}}), f_\sigma^2(\hat{\mathbf{z}})I)$. Here, $f_\mu(\cdot)$ and $f_\sigma(\cdot)$ are functions that estimate the mean and standard deviation of this Gaussian distribution, respectively.

Since KL divergence is always non-negative, we have $D_{\text{KL}}(p(\hat{\mathbf{z}}) || q(\hat{\mathbf{z}})) \geq 0$, which can derive the upper bound of $I(X; \hat{Z})$:

$$I(X; \hat{Z}) \leq \mathbb{E}_{\mathbf{a}, \mathbf{x}} [D_{\text{KL}}(p_\phi(\hat{\mathbf{z}}|\mathbf{x})||q(\hat{\mathbf{z}}))]. \quad (16)$$

The derivation of Eq. (16) is given in Appendix B. Therefore, we derive the following corollary as an approximation of Eq. (11).

Corollary 1. Assume the DPGM shown in Fig. 2, let $q_\psi(\mathbf{a}|\hat{\mathbf{z}}, \mathbf{m}, \mathbf{h})$ be a variational approximation of $p(\mathbf{a}|\hat{\mathbf{z}}, \mathbf{m}, \mathbf{h})$, let $q(\hat{\mathbf{z}}) \sim \mathcal{N}(\boldsymbol{\mu}_{\hat{\mathbf{z}}}, \boldsymbol{\sigma}_{\hat{\mathbf{z}}}^2 I)$ be a variational approximation of $p(\hat{\mathbf{z}})$, and let $p_\phi(\hat{\mathbf{z}}|\mathbf{x}) \sim \mathcal{N}(f_\mu(\hat{\mathbf{z}}), f_\sigma^2(\hat{\mathbf{z}})I)$ be a variational approximation of $p(\hat{\mathbf{z}}|\mathbf{x})$, the upper bound of Eq. (11) is given by

$$\begin{aligned} \mathcal{L}_{\text{VIB}} &:= \mathbb{E}_{\mathbf{a}, \mathbf{x}} \left\{ \mathbb{E}_{\hat{\mathbf{z}}|\mathbf{x}; \phi} \left[\mathbb{E}_{\mathbf{m}, \mathbf{h}} [-\log q_\psi(\mathbf{a}|\hat{\mathbf{z}}, \mathbf{m}, \mathbf{h})] \right] \right. \\ &\quad \left. + \beta D_{\text{KL}}(p_\phi(\hat{\mathbf{z}}|\mathbf{x})||q(\hat{\mathbf{z}})) \right\} \\ &\geq \mathcal{L}_{\text{IB}} + H(A). \end{aligned} \quad (17)$$

This corollary can be optimized using stochastic gradient descent through Monte Carlo sampling, providing a practical framework for empirical estimation and subsequent optimization. Given a dataset with size K_a , a mini-batch $\{(\mathbf{a}_i, \mathbf{x}_i)\}_{i=1}^{K_b}$ of size K_b is randomly drawn without overlap in the same epoch to compute the gradient of loss \mathcal{L}_{VIB} . In particular, the number of samples of $-\log q_\psi(\mathbf{a}|\hat{\mathbf{z}}, \mathbf{m}, \mathbf{h})$ can be set to 1 as long as the size of the dataset K_a is large enough [13]. Thus, we have the following estimation:

$$\begin{aligned} \mathcal{L}_{\text{VIB}} &\approx \frac{1}{K_b} \sum_{i=1}^{K_b} \left\{ -\log q_\psi(\mathbf{a}_i|\hat{\mathbf{z}}_i, \mathbf{m}_i, \mathbf{h}_i) \right. \\ &\quad \left. + \beta D_{\text{KL}}(p_\phi(\hat{\mathbf{z}}|\mathbf{x}_i)||q(\hat{\mathbf{z}})) \right\}. \end{aligned} \quad (18)$$

Note that the dataset $\{(\mathbf{a}_i, \mathbf{x}_i)\}_{i=1}^{K_a}$ can be collected from expert agents or human drivers.

V. DELAY-AWARE TRAJECTORY-GUIDED CONTROL PREDICTION

Trajectory-Guided Control Prediction (TGCP) is one of the state-of-the-art frameworks of E2E autonomous driving, integrating trajectory planning and multistage control prediction

together [49]. This advanced framework, which uses only a monocular camera, currently ranks third on the Car Learning to Act (CARLA) leaderboard¹. However, the original TGCP framework relies on a stream of raw images for decision making, resulting in high bandwidth usage. In addition, it does not account for the impact of communication latency on decision-making processes.

To overcome these limitations, we have developed a Delay-aware Trajectory-guided Control Prediction (DTCP) strategy that integrates the trajectory and control branches while considering the delay, as shown in Fig. 3. This integration ensures that predicted drive commands reduce the perceived E2E delay, leading to safer and more efficient autonomous driving.

We assume the system is time-slotted and initiates at the time $t = 0$. The duration of each time slot is denoted as τ . Let $\mathbf{z}_t^{l(t)}$ denote the transmitted JSCC symbols with length $l(t)$, and \mathbf{m}_t represents the state information, both corresponding to the image \mathbf{x}_t captured by the onboard camera at time t . The term $1 \leq l(t) \leq l_z$ denotes a function that decides the number of selected JSCC symbols of \mathbf{z}_t . For simplicity of notation, we denote $l(t)$ by l in the following formulation.

Define the index set $D_t \subset \{1, 2, \dots, l_z\}$ such that:

$$D_t = \{i \in \{1, \dots, l_z\} \mid |z_i^t|^2 \text{ is one of the } l \text{ largest numbers in } |z_t^t|^2\}. \quad (19)$$

In particular, $\mathbf{z}_t^l = \{z_i^t \mid i \in D_t\}$ are JSCC symbols selected from $\mathbf{z}_t = [z_1^t, \dots, z_{l_z}^t]$ based on energy significance. The selected JSCC symbols are kept for transmission, while the missing JSCC symbols are filled with 0 on the edge server. Note that this selection process can be integrated into the JSCC encoder f_e . If only selected JSCC symbols are transmitted, the receiver must be made aware of the indices of the selected or abandoned JSCC symbols, which may increase the communication load. In this work, we design the selective JSCC symbols to provide flexibility within this task-oriented communication co-designed paradigm and demonstrate their potential for dimensionality reduction. To address the additional communication load introduced by index transmission, methods such as Variable-Length Variational Feature Encoding (VL-VFE) [12] offer promising directions for further exploration.

A. Prediction for End-to-End Delay

In edge-enabled autonomous systems, drive commands are often outdated due to E2E delay, including communication, computation, and control delays. Fig. 4 shows a complete cycle of the communication, computing, and control process, along with the prediction structure. Assume that an image \mathbf{x}_{t_0} is captured by the camera at time $t = t_0$. After encoding and selecting, the JSCC symbols $\mathbf{z}_{t_0}^l$ are generated with a computation delay δ_e . The JSCC symbols reconstructed by the edge server are denoted as $\hat{\mathbf{z}}_{t_0}^l$ arriving with an uplink delay δ_u . The agent on the edge server takes δ_a time slots to generate the command $\mathbf{c}_{t_0+l_p}^{\text{comb}}$, where $l_p \geq 0$ denotes the prediction horizon. The command is then sent back to the vehicle with a downlink

¹ <https://leaderboard.carla.org/leaderboard/>

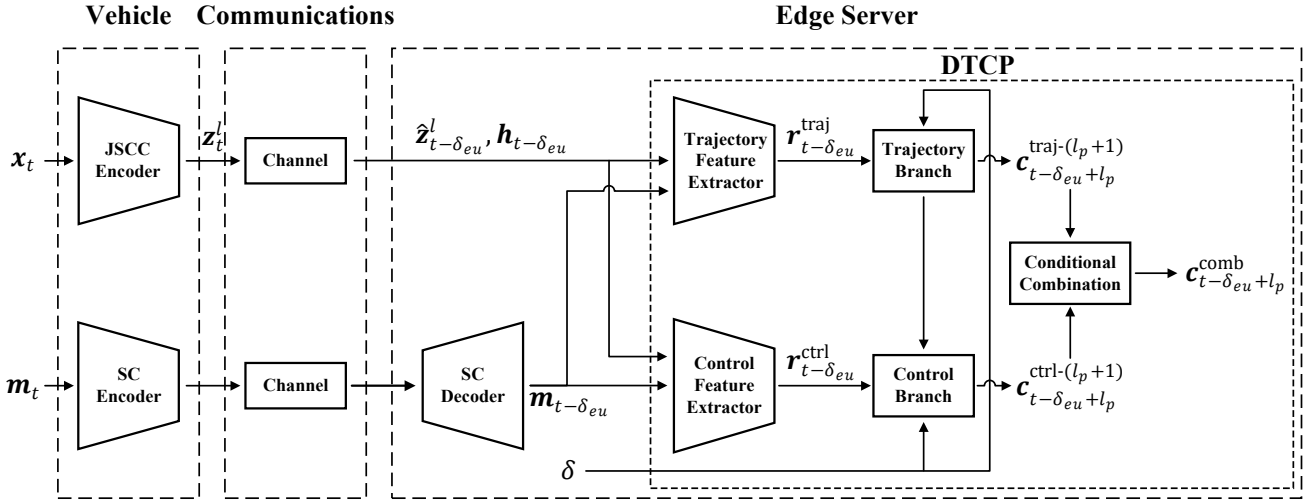


Fig. 3. The proposed task-oriented co-design framework based on JSCC and DTCP.

delay δ_d . Upon receiving the command, the vehicle takes δ_c time slots to execute the command. Thus, the E2E delay is expressed as $\delta = \delta_e + \delta_u + \delta_a + \delta_d + \delta_c$. Consequently, the perceived E2E delay is given by $\delta - l_p$. Since the command $c_{t_0+l_p}^{comb}$ consumes negligible bandwidth, it is assumed to be transmitted losslessly to the vehicle in this work. It is worth noting that while the uplink delay can be further decomposed into components such as transmission delay, queuing delay, propagation delay, and processing delay, a detailed analysis of each individual component lies outside the primary scope of this work. Instead, our focus is on the E2E delay and addressing it through predictive mechanisms.

It is crucial to recognize that in the process described above, when the onboard camera captures an image x_t at any time t , reconstructed JSCC symbols $\hat{z}_{t-\delta_{eu}}^l$ (corresponding to image $x_{t-\delta_{eu}}$) on the edge server are outdated of $\delta_{eu} = \delta_e + \delta_u$ time slots. The combined delay δ_{eu} can be calculated from the timestamp in the state information $m_{t-\delta_{eu}}$, if it is transmitted in sync with $\hat{z}_{t-\delta_{eu}}^l$. In addition, we assume that the agent's computation delay δ_a and the control execution delay δ_c are known constants, and the edge server continuously measures the downlink communication delay in real time. With this information, the agent remains aware of the E2E delay δ , allowing it to dynamically adjust the prediction horizon.

B. Trajectory Branch

The trajectory branch first generates planned waypoints, and then a low-level PID controller generates trajectory commands based on them. We define the function of the trajectory feature extractor as:

$$f_{\text{feat-t}} : \mathcal{Z} \times \mathcal{M} \times \mathcal{H} \rightarrow \mathcal{R}_{\text{traj}} \\ : (\hat{z}_{t-\delta_{eu}}^l, m_{t-\delta_{eu}}, h_{t-\delta_{eu}}) \mapsto r_{t-\delta_{eu}}^{\text{traj}}, \quad (20)$$

where $\hat{z}_{t-\delta_{eu}}^l$, $m_{t-\delta_{eu}}$, and $h_{t-\delta_{eu}}$ represent the reconstructed JSCC symbols, state information, and channel state, respectively, corresponding to image $x_{t-\delta_{eu}}$ captured by the camera δ_{eu} time slots ago. At time t , the trajectory feature on

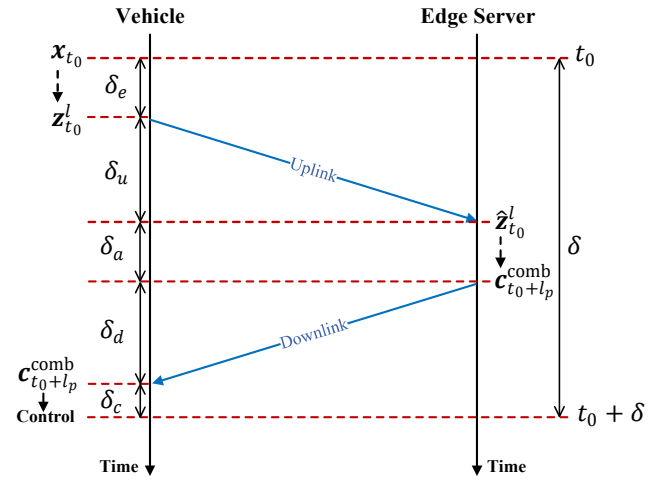


Fig. 4. The illustration of a completed cycle of the communication, computing, and control process, along with the prediction structure.

the edge server is denoted as $r_{t-\delta_{eu}}^{\text{traj}}$, as shown in Fig. 5. The trajectory hidden state $h_{t-\delta_{eu}}^{\text{traj}}$ of a Gated Recurrent Unit (GRU) [50] is initialized with the trajectory feature. Then it auto-regressively generates the sequence of trajectory hidden states $h_{t-\delta_{eu}+l_p+l_w}^{\text{traj}-(l_p+l_w)} = (h_{t-\delta_{eu}+l_p+l_w}^{\text{traj}}, \dots, h_{t-\delta_{eu}+1}^{\text{traj}})$, where l_w denotes an extra prediction horizon for planned waypoints and $l_p + l_w$ in the superscript represents the length of the sequence. Using a waypoint inference network, the planned $l_p + l_w$ waypoints can be obtained from the sequence of trajectory hidden states, denoted as $w_{t-\delta_{eu}+l_p+l_w}^{l_p+l_w} = (w_{t-\delta_{eu}+l_p+l_w}, \dots, w_{t-\delta_{eu}+1})$. The initial waypoint $w_{t-\delta_{eu}}$ is defined as the origin.

Each trajectory $w_{t-i+l_w}^{l_w+1} = (w_{t-i+l_w}, \dots, w_{t-i})$ with length $l_w + 1$ is processed by a PID controller to generate the predicted trajectory command c_{t-i}^{traj} , where $i = \delta_{eu}, \dots, \delta_{eu} - l_p$. Thus, the sequence of predicted trajectory commands branch is denoted as $c_{t-\delta_{eu}+l_p}^{\text{traj}-(l_p+1)} = (c_{t-\delta_{eu}+l_p}^{\text{traj}}, \dots, c_{t-\delta_{eu}}^{\text{traj}})$. We

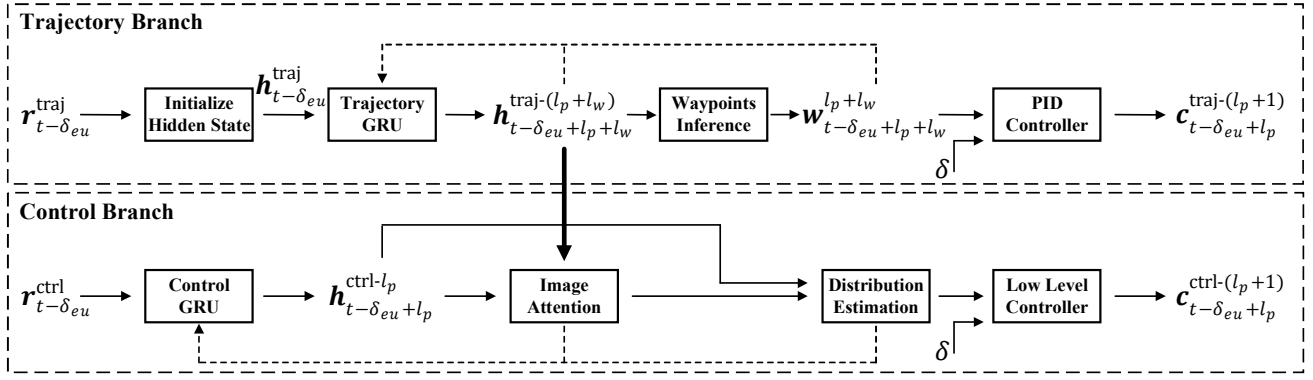


Fig. 5. The framework of the trajectory and control branch of DTCP.

defined the function of the trajectory branch as:

$$f_{\text{traj}} : \mathcal{R}_{\text{traj}} \rightarrow \mathcal{C}_{\text{cmd}}^{l_p+1} : \mathbf{r}_{t-\delta_{eu}}^{\text{traj}} \mapsto \mathbf{c}_{t-\delta_{eu}+l_p}^{\text{traj}-(l_p+1)}. \quad (21)$$

C. Control Branch

As outlined in [49], a control model that predicts current actions based solely on current inputs typically employs supervised training similar to behavior cloning, which assumes that the data is i.i.d. However, for autonomous driving, future states and commands are under the influence of historical commands. To address this problem and deal with latency, the control branch predicts control commands in multiple steps in the future and obtains the desired commands based on the E2E delay δ .

We defined the mapping of the reconstructed JSCC symbols to the control features as:

$$f_{\text{feat-c}} : \mathcal{Z} \times \mathcal{M} \times \mathcal{H} \rightarrow \mathcal{R}_{\text{ctrl}} : (\hat{\mathbf{z}}_{t-\delta_{eu}}^l, \mathbf{m}_{t-\delta_{eu}}, \mathbf{h}_{t-\delta_{eu}}) \mapsto \mathbf{r}_{t-\delta_{eu}}^{\text{ctrl}}. \quad (22)$$

At time t , the control hidden state $\mathbf{h}_{t-\delta_{eu}}^{\text{ctrl}}$ is initialized with zero value and enters control GRU with the control feature $\mathbf{r}_{t-\delta_{eu}}^{\text{ctrl}}$ to generate the next hidden state $\mathbf{h}_{t-\delta_{eu}+1}^{\text{ctrl}}$. The hidden state of the control branch $\mathbf{h}_{t-\delta_{eu}+1}^{\text{ctrl}}$ and the hidden state of the trajectory branch $\mathbf{h}_{t-\delta_{eu}+1}^{\text{traj}}$ are used to estimate the important regions of the image by generating a binary mask that matches the shape of the image feature map from the middle layer of the control feature extractor [49]. This mask is then applied through element-wise multiplication with the feature map. The results of image attention are then used to generate the predicted control feature $\mathbf{r}_{t-\delta_{eu}+1}^{\text{ctrl}}$ and the control command $\mathbf{c}_{t-\delta_{eu}+1}^{\text{ctrl}}$. The next control GRU hidden state $\mathbf{h}_{t-\delta_{eu}+2}^{\text{ctrl}}$ is obtained from the previous hidden state $\mathbf{h}_{t-\delta_{eu}+1}^{\text{ctrl}}$ and the predicted control feature $\mathbf{r}_{t-\delta_{eu}+1}^{\text{ctrl}}$. This process auto-regressively generates the sequence of control hidden states $\mathbf{h}_{t-\delta_{eu}+l_p}^{\text{ctrl-l}_p} = (\mathbf{h}_{t-\delta_{eu}+l_p}^{\text{ctrl}}, \dots, \mathbf{h}_{t-\delta_{eu}+1}^{\text{ctrl}})$, which is used to generate the sequence of predicted control features $\mathbf{r}_{t-\delta_{eu}+l_p}^{\text{ctrl-l}_p} = (\mathbf{r}_{t-\delta_{eu}+l_p}^{\text{ctrl}}, \dots, \mathbf{r}_{t-\delta_{eu}+1}^{\text{ctrl}})$. Based on that, the sequence of predicted control commands $\mathbf{c}_{t-\delta_{eu}+l_p}^{\text{ctrl}-(l_p+1)} = (\mathbf{c}_{t-\delta_{eu}+l_p}^{\text{ctrl}}, \dots, \mathbf{c}_{t-\delta_{eu}}^{\text{ctrl}})$ is derived from a low-level controller, where $\mathbf{c}_{t-\delta_{eu}}^{\text{ctrl}}$ is directly generated from the initial control

feature $\mathbf{r}_{t-\delta_{eu}}^{\text{ctrl}}$. The function of the trajectory branch is defined as:

$$f_{\text{ctrl}} : \mathcal{R}_{\text{ctrl}} \times \mathcal{H}_{\text{traj}}^{l_p} \rightarrow \mathcal{C}_{\text{cmd}}^{l_p+1} : (\mathbf{r}_{t-\delta_{eu}}^{\text{ctrl}}, \mathbf{h}_{t-\delta_{eu}+l_p}^{\text{traj-l}_p}) \mapsto \mathbf{c}_{t-\delta_{eu}+l_p}^{\text{ctrl}-(l_p+1)}. \quad (23)$$

D. Two Branch Combination

To minimize the perceived E2E delay δ_r , $l_p \geq \delta$ must be satisfied, i.e., $l_p - \delta_{eu} \geq \delta_a + \delta_d + \delta_c$. Because the trajectory branch and the control branch specialize in different driving scenarios, commands from the two branches are conditionally fused to obtain the combined command $\mathbf{c}_{t-\delta_{eu}+l_p}^{\text{comb}}$. This fusion depends on the driving situation – whether the vehicle is turning or not. In addition, considering the trade-off between the prediction horizon and the reliability of the system, the predicted control is applied when the delay exceeds a certain threshold δ_T for the turning situation. Otherwise, the robustness of the system can deal with the delay better than applying predicted commands. We define this combination function as:

$$f_{\text{comb}} : \mathcal{C}_{\text{cmd}}^{l_p+1} \times \mathcal{C}_{\text{cmd}}^{l_p+1} \rightarrow \mathcal{C}_{\text{cmd}} : (\mathbf{c}_{t-\delta_{eu}+l_p}^{\text{traj}-(l_p+1)}, \mathbf{c}_{t-\delta_{eu}+l_p}^{\text{ctrl}-(l_p+1)}) \mapsto \mathbf{c}_{t-\delta_{eu}+l_p}^{\text{comb}}. \quad (24)$$

The combined command $\mathbf{c}_{t-\delta_{eu}+l_p}^{\text{comb}}$ is denoted as:

$$\mathbf{c}_{t-\delta_{eu}+l_p}^{\text{comb}} = \begin{cases} \lambda_c \cdot \mathbf{c}_{t-\delta_{eu}+l_p}^{\text{traj}} + (1 - \lambda_c) \cdot \mathbf{c}_{t-\delta_{eu}+l_p}^{\text{ctrl}}, & \text{if turning and } \delta \geq \delta_T, \\ \lambda_c \cdot \mathbf{c}_{t-\delta_{eu}}^{\text{traj}} + (1 - \lambda_c) \cdot \mathbf{c}_{t-\delta_{eu}}^{\text{ctrl}}, & \text{if turning and } \delta < \delta_T, \\ \lambda_c \cdot \mathbf{c}_{t-\delta_{eu}}^{\text{ctrl}} + (1 - \lambda_c) \cdot \mathbf{c}_{t-\delta_{eu}}^{\text{traj}}, & \text{otherwise,} \end{cases} \quad (25)$$

where $\lambda_c \in [0.5, 1]$ is a hyperparameter. The details of a complete cycle of communication, computing, and control of DTCP and task-oriented JSCC are illustrated in Algorithm 1.

Algorithm 1 Communication, Computing, and Control of DTCP and Task-Oriented JSCC.

- 1: **Initialization:** Load the pre-trained parameter ϕ for JSCC encoder (f_e) and parameter ψ for DTCP ($f_{\text{feat-t}}, f_{\text{feat-c}}, f_{\text{traj}}$, and f_{ctrl}).
 - 2: **Vehicle:**
 - 3: At time $t - \delta_{eu}$, capture image $\mathbf{x}_{t-\delta_{eu}}$ and generate state information $\mathbf{m}_{t-\delta_{eu}}$.
 - 4: At time $t - \delta_u$, generate selected JSCC symbols:
 $\mathbf{z}_{t-\delta_{eu}}^l \leftarrow f_e(\mathbf{x}_{t-\delta_{eu}})$.
 - 5: **Edge Server:**
 - 6: At time t , receive reconstructed JSCC symbols
 $\hat{\mathbf{z}}_{t-\delta_{eu}}^l \leftarrow f_h(\mathbf{z}_{t-\delta_{eu}}^l)$ and state information $\mathbf{m}_{t-\delta_{eu}}$. Measure corresponding channel state $\mathbf{h}_{t-\delta_{eu}}$.
 - 7: Generate trajectory feature:
 $\mathbf{r}_{t-\delta_{eu}}^{\text{traj}} \leftarrow f_{\text{feat-t}}(\hat{\mathbf{z}}_{t-\delta_{eu}}^l, \mathbf{m}_{t-\delta_{eu}}, \mathbf{h}_{t-\delta_{eu}})$.
 - 8: Generate sequence of trajectory command:
 $\mathbf{c}_{t-\delta_{eu}+l_p}^{\text{traj-(}l_p+1)} \leftarrow f_{\text{traj}}(\mathbf{r}_{t-\delta_{eu}}^{\text{traj}})$, and sequence of hidden state $\mathbf{h}_{t-\delta_{eu}+l_p}^{\text{traj-}l_p}$.
 - 9: Generate control feature:
 $\mathbf{r}_{t-\delta_{eu}}^{\text{ctrl}} \leftarrow f_{\text{feat-c}}(\hat{\mathbf{z}}_{t-\delta_{eu}}^l, \mathbf{m}_{t-\delta_{eu}}, \mathbf{h}_{t-\delta_{eu}})$.
 - 10: Generate sequence of control command:
 $\mathbf{c}_{t-\delta_{eu}+l_p}^{\text{ctrl-(}l_p+1)} \leftarrow f_{\text{ctrl}}(\mathbf{r}_{t-\delta_{eu}}^{\text{ctrl}}, \mathbf{h}_{t-\delta_{eu}+l_p}^{\text{traj-}l_p})$.
 - 11: At time $t + \delta_a$, generate combined command:
 $\mathbf{c}_{t-\delta_{eu}+l_p}^{\text{comb}} \leftarrow f_{\text{comb}}(\mathbf{c}_{t-\delta_{eu}+l_p}^{\text{traj-(}l_p+1)}, \mathbf{c}_{t-\delta_{eu}+l_p}^{\text{ctrl-(}l_p+1)})$.
 - 12: **Vehicle:**
 - 13: At time $t + \delta_a + \delta_d$, receive command $\mathbf{c}_{t-\delta_{eu}+l_p}^{\text{comb}}$.
 - 14: At time $t + \delta_a + \delta_d + \delta_c$, vehicle is controlled by the command $\mathbf{c}_{t-\delta_{eu}+l_p}^{\text{comb}}$.
-

E. Loss function

We denote the estimated action corresponding to image $\mathbf{x}_{t-\delta_{eu}}$ by

$$\hat{\mathbf{a}}_{t-\delta_{eu}} = (v_{t-\delta_{eu}}, s_{t-\delta_{eu}}, \mathbf{w}_{t-\delta_{eu}+l_p+l_w}^{l_p+l_w}, \mathbf{r}_{t-\delta_{eu}}^{\text{traj}}, \mathbf{c}_{t-\delta_{eu}+l_p}^{\text{ctrl-(}l_p+1)}, \mathbf{r}_{t-\delta_{eu}+l_p}^{\text{ctrl-(}l_p+1)}), \quad (26)$$

which consists of task-critical variables, where $v_{t-\delta_{eu}}$ denotes the estimated target velocity and $s_{t-\delta_{eu}}$ denotes the value of the extracted features. The corresponding ground-truth action is defined as:

$$\mathbf{a}_{t-\delta_{eu}} = (\text{ex } v_{t-\delta_{eu}}, \text{ex } s_{t-\delta_{eu}}, \text{ex } \mathbf{w}_{t-\delta_{eu}+l_p+l_w}^{l_p+l_w}, \text{ex } \mathbf{r}_{t-\delta_{eu}}^{\text{traj}}, \text{ex } \mathbf{c}_{t-\delta_{eu}+l_p}^{\text{ctrl-(}l_p+1)}, \text{ex } \mathbf{r}_{t-\delta_{eu}+l_p}^{\text{ctrl-(}l_p+1)}), \quad (27)$$

which is collected from expert agents or human drivers.

The loss function of the trajectory branch is defined as follows:

$$\mathcal{L}_{\text{traj}} = \|\mathbf{w}_{t-\delta_{eu}+l_p+l_w}^{l_p+l_w} - \text{ex } \mathbf{w}_{t-\delta_{eu}+l_p+l_w}^{l_p+l_w}\|_1 + \lambda_{\text{feat}} \|\mathbf{r}_{t-\delta_{eu}}^{\text{traj}} - \text{ex } \mathbf{r}_{t-\delta_{eu}}^{\text{traj}}\|_2, \quad (28)$$

where λ_{feat} is a hyperparameter, $\|\cdot\|_1$ denotes the ℓ_1 -norm, $\|\cdot\|_2$ denotes the Euclidean distance (ℓ_2 -norm).

For the control branch, the distribution of the control action is modeled as a beta distribution [49]. The loss function of the

control branch is defined as follows:

$$\mathcal{L}_{\text{ctrl}} = \frac{1}{l_p + 1} \sum_{i=t-\delta_{eu}}^{t-\delta_{eu}+l_p} D_{\text{KL}}(\mathcal{B}e(\mathbf{c}_i^{\text{ctrl}}) \|\| \mathcal{B}e(\text{ex } \mathbf{c}_i^{\text{ctrl}})) + \lambda_{\text{feat}} \|\mathbf{r}_{t-\delta_{eu}+l_p}^{\text{ctrl-(}l_p+1)} - \text{ex } \mathbf{r}_{t-\delta_{eu}+l_p}^{\text{ctrl-(}l_p+1)}\|_2, \quad (29)$$

where $\mathcal{B}e(\cdot)$ denotes the beta distribution. Furthermore, an auxiliary function is used to measure the accuracy of the estimated current speed and value that is obtained from the speed head and the value head, respectively, to help the agent make decisions [49]. The auxiliary function is defined as:

$$\mathcal{L}_{\text{aux}} = \lambda_{\text{value}} \|v_{t-\delta_{eu}} - \text{ex } v_{t-\delta_{eu}}\|_1 + \lambda_{\text{speed}} \|s_{t-\delta_{eu}} - \text{ex } s_{t-\delta_{eu}}\|_2, \quad (30)$$

where λ_{value} and λ_{speed} are hyperparameters. Thus, the overall loss function of the DTCP is defined as:

$$\mathcal{L}_{\text{DTCP}} = \lambda_{\text{traj}} \mathcal{L}_{\text{traj}} + \lambda_{\text{ctrl}} \mathcal{L}_{\text{ctrl}} + \lambda_{\text{aux}} \mathcal{L}_{\text{aux}}, \quad (31)$$

where λ_{traj} , λ_{ctrl} , and λ_{aux} are hyperparameters. The design of the loss functions in Eq. (28), Eq. (29), and Eq. (30) follows a consistent principle: combining an output loss and a feature loss through a weighted summation. We consider these weights essential because the two types of variables (e.g., waypoints and trajectory features) typically have different scales and ranges, requiring proper balancing to ensure meaningful contributions from each term. For the overall loss function in Eq. (31), the weights (λ_{traj} , λ_{ctrl} , λ_{aux}) are carefully chosen to ensure that each component contributes appropriately to the task objective, aligning with the goal of achieving better system performance.

F. Joint Training

To jointly train the DTCP and task-oriented JSCC, we employ imitation learning, specifically through behavior cloning. In this approach, the agent learns to perform tasks by replicating the actions of experts based on a dataset of expert demonstrations. Behavior cloning works by directly mapping observed states to corresponding actions, allowing the agent to learn a policy that mirrors the expert's behavior. This approach is particularly effective in scenarios where a large amount of labeled data is available, allowing the agent to generalize from the expert's actions to similar situations encountered during autonomous driving.

Assuming the posterior $q_\psi(\mathbf{a} | \hat{\mathbf{z}}, \mathbf{m}, \mathbf{h})$ follows a Gaussian distribution $\mathcal{N}(\mu_\psi(\hat{\mathbf{z}}, \mathbf{m}, \mathbf{h}), \sigma_{\text{const}}^2 I)$, where $\mu_\psi(\hat{\mathbf{z}}, \mathbf{m}, \mathbf{h})$ maps reconstructed JSCC symbols $\hat{\mathbf{z}}$, state information \mathbf{m} , and channel state \mathbf{h} to the mean of a Gaussian distribution and σ_{const} is a constant, we can derive the following expression:

$$-\log q_\psi(\mathbf{a} | \hat{\mathbf{z}}, \mathbf{m}, \mathbf{h}) \sim \frac{1}{2\sigma_{\text{const}}^2} \|\mathbf{a} - \mu_\psi(\hat{\mathbf{z}}, \mathbf{m}, \mathbf{h})\|_2^2, \quad (32)$$

where $\mu_\psi(\hat{\mathbf{z}}, \mathbf{m}, \mathbf{h}) = \hat{\mathbf{a}}$. Eq. (32) shows that $-\log q_\psi(\mathbf{a} | \hat{\mathbf{z}}, \mathbf{m}, \mathbf{h})$ can serve as a distance metric, analogous to the square of the ℓ^2 -norm. From this perspective, we heuristically regard the loss function of DTCP as an extension

Algorithm 2 Joint Training of DTCP and Task-Oriented JSCC.

Initialization: Initialize the neural network parameters ϕ and ψ .

- 1: **Input:** Image dataset \mathcal{X} with corresponding ground-truth agent output \mathcal{A} and state information \mathcal{M} .
- 2: **while** not converged **do**
- 3: Sample mini-batch $\{(\mathbf{a}_i, \mathbf{x}_i)\}_{i=1}^{K_b}$ from \mathcal{A} and \mathcal{X} with corresponding state information $\{\mathbf{m}_i\}_{i=1}^{K_b}$ from \mathcal{M} .
- 4: **for** sample $i = 1, \dots, K_b$ **do**
- 5: Encode image to JSCC symbols: $\mathbf{z}_i \leftarrow f_e(\mathbf{x}_i)$.
- 6: Transmit JSCC symbols through channel and apply equalization: $\hat{\mathbf{z}}_i \leftarrow f_h(\mathbf{z}_i)$.
- 7: Estimate mean and standard deviation:
 $\boldsymbol{\mu}_i \leftarrow f_\mu(\hat{\mathbf{z}}_i)$, $\boldsymbol{\sigma}_i \leftarrow f_\sigma(\hat{\mathbf{z}}_i)$.
- 8: Compute KL divergence $D_{\text{KL}}(p_\phi(\hat{\mathbf{z}}|\mathbf{x}_i)||q(\hat{\mathbf{z}}))$.
- 9: Generate estimated action: $\hat{\mathbf{a}}_i \leftarrow f_a(\hat{\mathbf{z}}_i, \mathbf{m}_i, \mathbf{h}_i)$.
- 10: Compute DTCP loss based on Eq. (31).
- 11: **end for**
- 12: Compute joint loss $\mathcal{L}'_{\text{VIB}}$ of this mini-batch based on Eq. (33).
- 13: Update neural network parameters: $\phi \leftarrow \phi - \nabla_\phi \mathcal{L}'_{\text{VIB}}$,
 $\psi \leftarrow \psi - \nabla_\psi \mathcal{L}'_{\text{VIB}}$.
- 14: **end while**

of the first term in Eq. (18), thus we can jointly optimize DTCP with task-oriented communication as follows:

$$\mathcal{L}'_{\text{VIB}} := \frac{1}{K_b} \sum_{i=1}^{K_b} \{ \mathcal{L}_{\text{DTCP}} + \beta D_{\text{KL}}(p_\phi(\hat{\mathbf{z}}|\mathbf{x}_i)||q(\hat{\mathbf{z}})) \}. \quad (33)$$

The joint training process of proposed task-oriented co-design is shown in Algorithm 2.

VI. PERFORMANCE EVALUATION

In this section, we present a case study of our proposed task-oriented co-design framework. The evaluation is carried out within the simulator CARLA, which offers a variety of urban environments that closely mimic real-world traffic scenarios.

A. Experimental Setup

a) Dataset: We utilize the well-structured dataset provided by [49], which consists of images (height = 256, width = 900, channels = 3) captured from various urban environments, along with the corresponding vehicle state information. Specifically, the dataset contains $K_a = 189524$ images from four maps (Town01, Town03, Town04, and Town06) for training, and 27201 images from four different maps (Town02, Town05, Town07, and Town10) for testing. This well-structured dataset allows us to effectively train and validate the proposed framework across a range of real-world-like scenarios.

To train DTCP using behavior cloning, we use Roach [51] as the expert agent in our experiments. Roach is a highly capable autonomous driving agent that relies on Bird's-eye View (BEV) as input. Since BEV data are challenging to collect in real time for real-world autonomous driving, this highlights the importance of training autonomous driving agents using data from standard sensors. Our proposed DTCP, equipped with

only one camera, demonstrates strong potential for practical deployment in real-world scenarios.

b) Evaluation: The experiment is designed to evaluate the driving performance of the proposed task-oriented co-design framework against established baselines under varying communication conditions. These conditions include significant communication latency, constrained bandwidth, and the presence of noisy fading channels. The baselines for comparison include three widely recognized image coding techniques: 1) JPEG [16]; 2) JPEG2000 [17]; and 3) BPG [52]. Each coding method is followed by (2048, 6144) Low-Density Parity-Check (LDPC) codes with a 64-QAM digital modulation scheme.

In addition, two JSCC-based methods, referred to as ‘‘JSCC-AE’’ [6] and ‘‘JSCC-VAE’’ [53], are also included as baselines. JSCC-AE is a seminal work that introduced the concept of joint source-channel coding without relying on explicit separate codes for compression or error correction, making it a foundational approach in this area. Based on this, JSCC-VAE offers robustness against variations in channel conditions, further enhancing its practical applicability. These methods focus on accurately reconstructing the image at the edge server, but do not co-design with the autonomous driving agent (DTCP). Furthermore, the baseline includes [49], which performs driving tasks using uncompressed images, denoted as ‘‘TGCP.’’

Driving performance is quantified using the established driving score metric² of CARLA, which evaluates the vehicle’s ability to follow predefined waypoints, reach target destinations, and comply with traffic regulations. To ensure robustness, each experiment is repeated three times on a selected route in Town05, under four distinct weather conditions: clear noon, cloudy sunset, soft rain at dawn, and heavy rain at night. For a more intuitive comparison, we select road sections where TGCP achieves a perfect driving score of 100.

c) Parameters Settings: For the task-oriented JSCC encoder, we configure the dimension of the JSCC symbols to $l_z = 1024$, achieving a significant low bandwidth compression ratio of $l_z/l_x \approx 0.0015$. The average power constraint P_{target} for JSCC symbols is fixed at 1. The predefined Gaussian distribution is assumed to be $q(\hat{\mathbf{z}}) \sim \mathcal{N}(0, I)$. In addition, ‘‘JSCC-AE’’ and ‘‘JSCC-VAE’’ use the same network structure as the proposed task-oriented JSCC for fair comparisons.

For DTCP, the parameters are configured as follows: $\lambda_c = 0.7$, $\lambda_{\text{feat}} = 0.05$, $\lambda_{\text{value}} = 0.001$, $\lambda_{\text{speed}} = 0.05$, and $\lambda_{\text{traj}} = \lambda_{\text{ctrl}} = \lambda_{\text{aux}} = 1$. The values of $\lambda_{[\cdot]}$ were selected based on our preliminary tests, which ensure a stable training process and achieve relatively optimal driving performance. In our preliminary tests, we observed that excessively large ($\beta > 0.01$) or small ($\beta < 0.000001$) values of β can disrupt the balance between the IB terms, leading to training instability and crashes. To address this, we set $\beta = 0.0001$ for jointly training JSCC encoder and DTCP under the IB objective. This β value creates a reasonable balance between the two IB terms, ensuring stable training and achieving good overall performance. For the mini-batch, we set $K_b = 32$.

² <https://leaderboard.carla.org/>

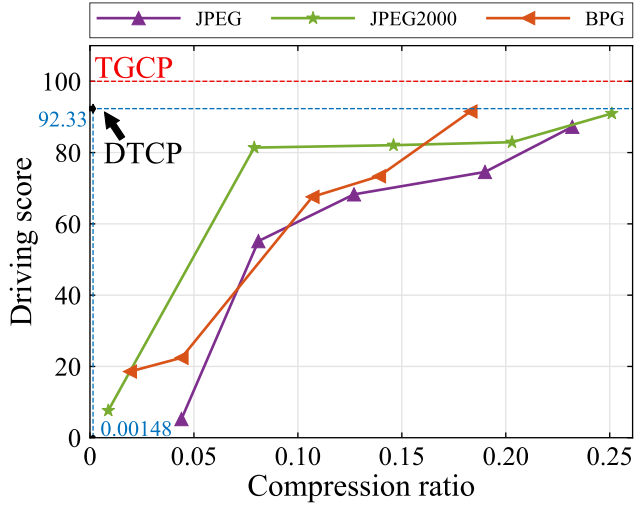


Fig. 7. Driving scores of traditional coding methods with varied bandwidth compression ratios under OFDM channel with SNR = 20 dB.

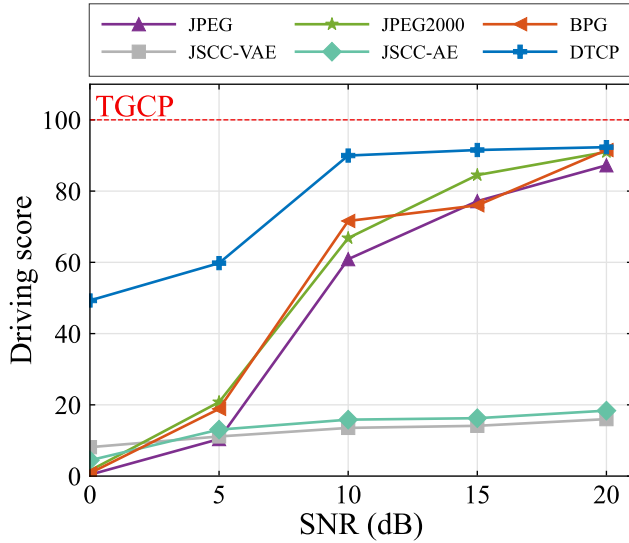


Fig. 8. Driving scores with varied SNRs under OFDM channel.

3) *Selection of JSCC symbols*: Given the characteristics of JSCC, symbols with relatively low energy are particularly vulnerable to noise. To optimize the trade-off between bandwidth compression and driving performance, we explore the selection of generated JSCC symbols, aiming to further reduce the bandwidth while maintaining the required driving performance.

As shown in Fig. 9, the number of selected JSCC symbols varies from 168 to 1008, in increments of 168, while the corresponding bandwidth compression ratio varies from 0.00024 to 0.00146. The choice of 168 as the incremental step size is based on the structure of a 5G resource block, which consists of 12 subcarriers and 14 OFDM symbols per slot, totaling 168 resource elements [54]. This value is a natural fit for our simulation setup, as it aligns with the granularity of resource allocation in modern cellular networks, making the

results more relevant for real-world applications.

The driving score exhibits a gradual decline (from 89.28 to 80.81) as the number of selected JSCC symbols decreases from 1008 to 504. However, the driving score drops sharply (from 80.81 to 52.15) when the number of selected JSCC symbols is reduced further from 504 to 168. This significant drop suggests that high-energy JSCC symbols are more critical to task performance, as they carry essential information required for accurate decision-making in autonomous driving tasks.

Our proposed DTCP framework demonstrates the ability to maintain a driving score above 80 by transmitting only the top 504 high-energy JSCC symbols. This selective transmission strategy demonstrates the potential to reduce communication overhead by 50.78% compared to transmitting 1024 JSCC symbols. Achieving this reduction depends on adequately mitigating index transmission overhead, which could be addressed by applying techniques such as VL-VFE [12]. This approach not only optimizes bandwidth usage but also ensures robust driving performance.

4) *Compensate Perceived E2E Delay*: The impact of communication delays on driving performance using the DTCP framework is presented in Fig. 10. The delay ranges from 0 to 20 time slots, increasing by increments of 2 time slots. We evaluate five distinct configurations within the DTCP framework:

- **DTCP-1**: Transmits all JSCC symbols and generates commands based on Eq. (25) with parameters $l = 1024$, $l_p = \delta$, and $\delta_T = 10$. This is also the default configuration of DTCP in previous experiments.
- **DTCP-2**: Selects 504 JSCC symbols for transmission, generating commands according to Eq. (25) with $l = 504$, $l_p = \delta$, and $\delta_T = 10$.
- **DTCP-3**: Transmits all JSCC symbols and always generates predicted commands for the turning situation ($l = 1024$, $l_p = \delta$, and $\delta_T = 0$).
- **DTCP-4**: Transmits all JSCC symbols but generates commands without prediction ($l = 1024$, $l_p = 0$, and $\delta_T \rightarrow \infty$).
- **DTCP-5**: Transmits all JSCC symbols and always generates predicted commands for all situations ($l = 1024$, $l_p = \delta$, and $\delta_T = 0$).

In this experiment, BPG with a bandwidth compression ratio of 0.183 is used as a representative baseline.

The results show that DTCP-5 experiences a steep decline in driving scores, falling below 61 even with a delay of just 2 time slots, and continues to decrease with increasing delay. In addition, DTCP-5 also performs worse than BPG in the presence of delays. These results indicate that relying exclusively on predicted commands is unreliable, particularly in non-turning scenarios.

When the delay is less than 10 time slots, DTCP-4 manages to maintain a driving score greater than 80 without relying on predicted commands. However, beyond 10 time slots, driving performance sharply declines, highlighting the limitations of unpredicted commands in high-latency conditions. In particular, when the delay is less than 8 time slots, the superior performance of DTCP-4 compared to DTCP-3 demonstrates that receiving accurate commands, even with some latency,

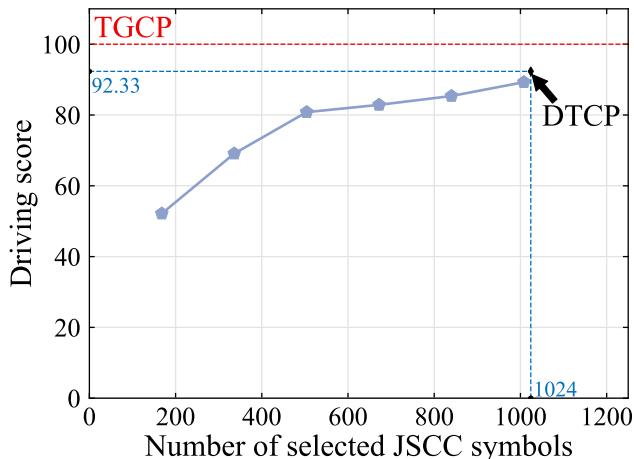


Fig. 9. Driving scores with varied selected JSCC symbols under OFDM channel with SNR = 20 dB.

is more critical than receiving inaccurate predicted commands under low latency. In contrast, when the delay exceeds 10 time slots, DTCP-3 outperforms DTCP-4, showing that adopting predicted commands becomes more effective in high-latency environments.

DTCP-1 combines the advantages of DTCP-3 and DTCP-4, offering the most balanced performance by dynamically switching between unpredicted and predicted commands based on E2E delay. It outperforms DTCP-4 and BPG significantly by 20.39 and 21.38 points at $\delta = 16$, 35.78 and 35.69 points at $\delta = 18$, and 26.95 and 31.59 points at $\delta = 20$, respectively. Furthermore, DTCP-1 outperforms DTCP-3 when the delay is less than 10 time slots.

DTCP-2, while leading to an average reduction of 17 points compared to DTCP-1, shows the potential to preserve 50.78% of communication resources. Despite the decrease in driving performance, DTCP-2 still maintains a driving score above 50, even with delays of up to 12 time slots. Furthermore, the driving scores of DTCP-2 exceed BPG and DTCP-4 when the delay is greater than 8 and 16 time slots, respectively, highlighting the efficiency of DTCP-2 in managing significant delays and offering a viable trade-off between communication bandwidth and driving performance.

VII. CONCLUSION

In this paper, we introduced a novel task-oriented co-design framework that integrates communication, computing, and control, specifically tailored for edge-enabled industrial CPS. By leveraging task-oriented JSCC through VIB theory, our approach effectively discards task-agnostic information, resulting in significant savings in communication bandwidth. Furthermore, with the incorporation of delay awareness into the trajectory-guided control prediction framework, the proposed DTCP framework adaptively generates predicted commands based on real-time delay, thereby maintaining driving performance even with significant latency.

Extensive evaluations using the CARLA simulator demonstrate that the task-oriented co-design framework significantly

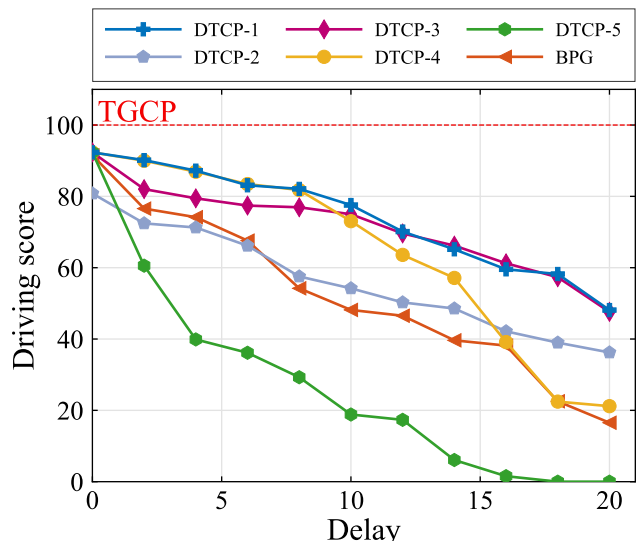


Fig. 10. Driving scores with varied delays under OFDM channel with SNR = 20 dB.

improves driving performance under conditions of constrained bandwidth, noise interference, and varying communication delays. The proposed DTCP consistently outperforms traditional methods across multiple scenarios. In particular, with an E2E delay of 1 second (equivalent to 20 time slots in CARLA), our framework achieves a driving score of 48.12, which is 31.59 points higher than when using BPG, while also reducing bandwidth usage by 99.19%. Moreover, our analysis of compensating for perceived E2E delay highlights the inherent unreliability of prediction under certain conditions, underscoring the need to balance predicted and unpredicted commands for optimal system performance. There are several promising directions for future research based on this work, such as extending the framework to more realistic wireless environments, including Urban Micro (UMi) and Urban Macro (UMa), and dynamically optimizing coding rates and modulation schemes based on channel conditions and SNR, leveraging 5G Modulation and Coding Scheme (MCS).

APPENDIX A

MODELING FREQUENCY-SELECTIVE CHANNEL

We consider a multipath fading channel described by a discrete channel transfer function:

$$\check{z}_{\text{time}} = \mathbf{h}_{\text{time}} * \mathbf{z}_{\text{time}} + \mathbf{n}_{\text{time}}, \quad (34)$$

where $*$ denotes the convolution operation. Here, \check{z}_{time} and \mathbf{z}_{time} are the received and transmitted signals in the time domain, respectively, while \mathbf{n}_{time} represents the additive Gaussian noise. The impulse response $\mathbf{h}_{\text{time}} = [h_{\text{time}-0}, \dots, h_{\text{time}-(N_{\text{path}}-1)}]$ captures the multipath effect, where $h_{\text{time}-i} \sim \mathcal{CN}(0, \sigma_i^2)$ for $i = 0, 1, \dots, N_{\text{path}} - 1$. We assume that path power decays exponentially as $\sigma_i^2 = \alpha_i e^{-\frac{i}{\gamma}}$, with α_i ensuring power normalization $\sum_{i=0}^{N_{\text{path}}-1} \sigma_i^2 = 1$. Here, γ is a delay spread constant.

To simplify, we assume synchronized transmission/reception without carrier frequency offset, and perfectly estimated chan-

nel state information by block-type pilot symbols. First, JSCC symbols $\mathbf{z} \in \mathbb{C}^{l_z}$ are padded with $N_{\text{sub}} - (l_z \bmod N_{\text{sub}})$ zeros and reshaped to $\mathbf{z}_r \in \mathbb{C}^{N_{\text{sym}} \times N_{\text{sub}}}$, where $N_{\text{sym}} = \lceil l_z / N_{\text{sub}} \rceil$ denotes the number of OFDM symbols and N_{sub} represents the number of subcarriers per OFDM symbol. When l_z / N_{sub} is not an integer, the subcarriers in the final OFDM symbol are not fully utilized for driving, but can be used for other tasks as needed.

Next, the Inverse Discrete Fourier Transform (IDFT) and cyclic prefix (CP) are applied, followed by transmission through the multipath channel as described in Eq. (34). The receiver removes the CP and applies the Discrete Fourier Transform (DFT) to yield the received JSCC symbols $\hat{\mathbf{z}}_r \in \mathbb{C}^{N_{\text{sym}} \times N_{\text{sub}}}$. Therefore, we have the following equation:

$$\hat{\mathbf{z}}_r[j, k] = \mathbf{h}_r[j, k] \mathbf{z}_r[j, k] + \mathbf{n}_r[j, k], \quad (35)$$

where k denotes the k th subcarrier, j denotes the j th OFDM symbol, and $\mathbf{h}_r[j, k] = \mathbf{h}_r[j', k], \forall j, j' \in \{1, \dots, N_{\text{sym}}\}$ represents the subcarrier-specific channel response. Flattening each term and removing the dimensions of driving-irrelevant subcarriers lead to the simplified expression:

$$\hat{\mathbf{z}} = \mathbf{h} \cdot \mathbf{z} + \mathbf{n},$$

where $\hat{\mathbf{z}} \in \mathbb{C}^{l_z}$, $\mathbf{h} \in \mathbb{C}^{l_z}$, and $\mathbf{n} \in \mathbb{C}^{l_z}$.

APPENDIX B DERIVATIONS OF (16)

The mutual information $I(X; \hat{Z})$ can be written as:

$$\begin{aligned} I(X; \hat{Z}) &= \int p(\mathbf{x}, \hat{\mathbf{z}}) \log \frac{p(\mathbf{x}, \hat{\mathbf{z}})}{p(\mathbf{x})p(\hat{\mathbf{z}})} d\mathbf{x} d\hat{\mathbf{z}} \\ &= \int p(\mathbf{x}, \hat{\mathbf{z}}) \log \frac{p_\phi(\hat{\mathbf{z}}|\mathbf{x})}{p(\hat{\mathbf{z}})} d\mathbf{x} d\hat{\mathbf{z}}. \end{aligned} \quad (36)$$

Since $D_{\text{KL}}(p(\hat{\mathbf{z}}) \| q(\hat{\mathbf{z}})) \geq 0$, we have

$$\int p(\hat{\mathbf{z}}) \log p(\hat{\mathbf{z}}) d\hat{\mathbf{z}} \geq \int p(\hat{\mathbf{z}}) \log q(\hat{\mathbf{z}}) d\hat{\mathbf{z}}. \quad (37)$$

So that

$$\begin{aligned} I(X; \hat{Z}) &\leq \int p(\mathbf{x}, \hat{\mathbf{z}}) \log \frac{p_\phi(\hat{\mathbf{z}}|\mathbf{x})}{q(\hat{\mathbf{z}})} d\mathbf{x} d\hat{\mathbf{z}} \\ &= \int p(\mathbf{a}, \mathbf{x}) p_\phi(\hat{\mathbf{z}}|\mathbf{x}) \log \frac{p_\phi(\hat{\mathbf{z}}|\mathbf{x})}{q(\hat{\mathbf{z}})} d\mathbf{a} d\mathbf{x} d\hat{\mathbf{z}} \\ &= \mathbb{E}_{\mathbf{a}, \mathbf{x}} [D_{\text{KL}}(p_\phi(\hat{\mathbf{z}}|\mathbf{x}) \| q(\hat{\mathbf{z}}))]. \end{aligned} \quad (38)$$

REFERENCES

- [1] C. She, C. Sun, Z. Gu, *et al.*, "A tutorial on ultrareliable and low-latency communications in 6G: Integrating domain knowledge into deep learning," *Proc. IEEE*, vol. 109, no. 3, pp. 204–246, 2021.
- [2] L. Chen, Y. Li, W. Silamu, Q. Li, S. Ge, and F.-Y. Wang, "Smart mining with autonomous driving in industry 5.0: Architectures, platforms, operating systems, foundation models, and applications," *IEEE Transactions on Intelligent Vehicles*, vol. 9, no. 3, pp. 4383–4393, 2024.
- [3] "Study on scenarios and requirements for next generation access technologies," document 3GPP, TSG RAN TR38.913 R14, 2017.
- [4] C. She, Y. Duan, G. Zhao, T. Q. S. Quek, Y. Li, and B. Vucetic, "Cross-layer design for mission-critical IoT in mobile edge computing systems," *IEEE Internet Things J.*, vol. 6, no. 6, pp. 9360–9374, 2019.
- [5] B. S. Khan, S. Jangsher, A. Ahmed, and A. Al-Dweik, "URLLC and eMBB in 5G industrial IoT: A survey," *IEEE Open J. Commun. Soc.*, vol. 3, pp. 1134–1163, 2022.
- [6] E. Boursoulatze, D. Burth Kurka, and D. Gündüz, "Deep joint source-channel coding for wireless image transmission," *IEEE Trans. on Cogn. Commun. Netw.*, vol. 5, no. 3, pp. 567–579, 2019.
- [7] D. B. Kurka and D. Gündüz, "DeepJSCC-f: Deep joint source-channel coding of images with feedback," *IEEE J. Sel. Areas Inf. Theory*, vol. 1, no. 1, pp. 178–193, 2020.
- [8] Y. Diao, Z. Meng, X. Xu, C. She, and P. G. Zhao, "Task-oriented source-channel coding enabled autonomous driving based on edge computing," in *Proc. IEEE Conf. Comput. Commun. Workshops*, 2024, pp. 1–6.
- [9] Z. Hou, C. She, Y. Li, L. Zhuo, and B. Vucetic, "Prediction and communication co-design for ultra-reliable and low-latency communications," *IEEE Trans. Wireless Commun.*, vol. 19, no. 2, pp. 1196–1209, 2020.
- [10] Z. Meng, C. She, G. Zhao, and D. De Martini, "Sampling, communication, and prediction co-design for synchronizing the real-world device and digital model in metaverse," *IEEE J. Sel. Areas Commun.*, vol. 41, no. 1, pp. 288–300, 2023.
- [11] Z. Meng, K. Chen, Y. Diao, *et al.*, "Task-oriented cross-system design for timely and accurate modeling in the metaverse," *IEEE J. Sel. Areas Commun.*, vol. 42, no. 3, pp. 752–766, 2024.
- [12] J. Shao, Y. Mao, and J. Zhang, "Learning task-oriented communication for edge inference: An information bottleneck approach," *IEEE J. Sel. Areas Commun.*, vol. 40, no. 1, pp. 197–211, 2022.
- [13] D. P. Kingma and M. Welling, "Auto-encoding variational bayes," *arXiv preprint arXiv:1312.6114*, 2013.
- [14] D. Gündüz, Z. Qin, I. E. Aguerri, *et al.*, "Beyond transmitting bits: Context, semantics, and task-oriented communications," *IEEE J. Sel. Areas Commun.*, vol. 41, no. 1, pp. 5–41, 2023.
- [15] D. B. Kurka and D. Gündüz, "Successive refinement of images with deep joint source-channel coding," in *Proc. IEEE Int. Workshop Signal Process. Adv. Wireless Commun.*, 2019, pp. 1–5.
- [16] G. Wallace, "The JPEG still picture compression standard," *IEEE Trans. Consum. Electron.*, vol. 38, no. 1, pp. 18–34, 1992.
- [17] D. S. Taubman, M. W. Marcellin, and M. Rabbani, "JPEG2000: Image compression fundamentals, standards and practice," *J. Electron. Imag.*, vol. 11, no. 2, pp. 286–287, 2002.
- [18] R. Gallager, "Low-density parity-check codes," *IRE Trans. Inf. Theory*, vol. 8, no. 1, pp. 21–28, 1962.
- [19] Y. Diao, Y. Zhang, P. G. Zhao, and D. De Martini, "TAGIC: Task-guided image communication framework for seamless teleoperation," in *Proc. IEEE Conf. Comput. Commun. Workshops*, 2024, pp. 1–2.
- [20] C. Chaccour, W. Saad, M. Debbah, Z. Han, and H. V. Poor, "Less data, more knowledge: Building next generation semantic communication networks," *IEEE Commun. Surv. Tut.*, pp. 1–1, 2024.
- [21] W. Yang, H. Du, Z. Q. Liew, *et al.*, "Semantic communications for future internet: Fundamentals, applications, and challenges," *IEEE Commun. Surv. Tut.*, vol. 25, no. 1, pp. 213–250, 2023.
- [22] E. C. Strinati, P. Di Lorenzo, V. Sciancalepore, *et al.*, "Goal-oriented and semantic communication in 6G AI-native networks: The 6G-GOALS approach," in *Proc. Joint Eur. Conf. Netw. Commun. 6G Summit*, 2024, pp. 1–6.
- [23] S. R. Pandey, V. P. Bui, and P. Popovski, "Goal-oriented communications in federated learning via feedback on risk-averse participation," in *Proc. IEEE Int. Symp. Pers. Indoor Mob. Radio Commun.*, 2023, pp. 1–6.
- [24] J. Kang, H. Du, Z. Li, *et al.*, "Personalized saliency in task-oriented semantic communications: Image transmission and performance analysis," *IEEE J. Sel. Areas Commun.*, vol. 41, no. 1, pp. 186–201, 2023.
- [25] N. Tishby, F. C. Pereira, and W. Bialek, "The information bottleneck method," in *Proc. Annu. Allerton Conf. Commun. Control Comput.*, 1999, pp. 368–377.
- [26] S. Arimoto, "An algorithm for computing the capacity of arbitrary discrete memoryless channels," *IEEE Trans. Inf. Theory*, vol. 18, no. 1, pp. 14–20, 1972.
- [27] R. Blahut, "Computation of channel capacity and rate-distortion functions," *IEEE Trans. Inf. Theory*, vol. 18, no. 4, pp. 460–473, 1972.
- [28] N. Tishby and N. Zaslavsky, "Deep learning and the information bottleneck principle," in *Proc. IEEE Inf. Theory Workshop*, 2015, pp. 1–5.
- [29] A. A. Alemi, I. Fischer, J. V. Dillon, and K. Murphy, "Deep variational information bottleneck," in *Proc. Int. Conf. Learn. Represent.*, 2017.
- [30] J. Shao, Y. Mao, and J. Zhang, "Task-oriented communication for multi-device cooperative edge inference," *IEEE Trans. Wireless Commun.*, vol. 22, no. 1, pp. 73–87, 2023.

- [31] Q. Liao and T.-Y. Tung, "AdaSem: Adaptive goal-oriented semantic communications for end-to-end camera relocalization," in *Proc. IEEE Conf. Comput. Commun.*, 2024, pp. 1111–1120.
- [32] Y. Shi, K. Yang, T. Jiang, J. Zhang, and K. B. Letaief, "Communication-efficient edge AI: Algorithms and systems," *IEEE Commun. Surv. Tut.*, vol. 22, no. 4, pp. 2167–2191, 2020.
- [33] E. Li, Z. Zhou, and X. Chen, "Edge intelligence: On-demand deep learning model co-inference with device-edge synergy," in *Proc. Workshop Mobile Edge Commun.*, 2018, pp. 31–36.
- [34] X. Huang and S. Zhou, "Dynamic compression ratio selection for edge inference systems with hard deadlines," *IEEE Internet Things J.*, vol. 7, no. 9, pp. 8800–8810, 2020.
- [35] W. Shi, Y. Hou, S. Zhou, Z. Niu, Y. Zhang, and L. Geng, "Improving device-edge cooperative inference of deep learning via 2-step pruning," in *Proc. IEEE Conf. Comput. Commun. Workshops*, 2019, pp. 1–6.
- [36] E. Li, L. Zeng, Z. Zhou, and X. Chen, "Edge AI: On-demand accelerating deep neural network inference via edge computing," *IEEE Trans. Wireless Commun.*, vol. 19, no. 1, pp. 447–457, 2020.
- [37] J. Shao and J. Zhang, "Communication-computation trade-off in resource-constrained edge inference," *IEEE Commun. Mag.*, vol. 58, no. 12, pp. 20–26, 2020.
- [38] J. Shao and J. Zhang, "BottleNet++: An end-to-end approach for feature compression in device-edge co-inference systems," in *Proc. IEEE Int. Conf. Commun. Workshops*, 2020, pp. 1–6.
- [39] M. Jankowski, D. Gündüz, and K. Mikolajczyk, "Joint device-edge inference over wireless links with pruning," in *Proc. IEEE Int. Workshop Signal Process. Adv. Wireless Commun.*, 2020, pp. 1–5.
- [40] M. Jankowski, D. Gündüz, and K. Mikolajczyk, "Wireless image retrieval at the edge," *IEEE J. Sel. Areas Commun.*, vol. 39, no. 1, pp. 89–100, 2021.
- [41] Y. Dubois, B. Bloem-Reddy, K. Ullrich, and C. J. Maddison, "Lossy compression for lossless prediction," in *Proc. Adv. Neural Inf. Process. Syst.*, vol. 34, 2021, pp. 14 014–14 028.
- [42] J. Shao, H. Zhang, Y. Mao, and J. Zhang, "Branchy-GNN: A device-edge co-inference framework for efficient point cloud processing," in *Proc. IEEE Int. Conf. Acoust., Speech, Signal Process.*, 2021, pp. 8488–8492.
- [43] M. Simsek, A. Aijaz, M. Dohler, J. Sachs, and G. Fettweis, "5G-enabled tactile internet," *IEEE J. Sel. Areas Commun.*, vol. 34, no. 3, pp. 460–473, 2016.
- [44] X. Tong, G. Zhao, M. A. Imran, Z. Pang, and Z. Chen, "Minimizing wireless resource consumption for packetized predictive control in real-time cyber physical systems," in *Proc. IEEE Int. Conf. Commun. Workshops*, 2018, pp. 1–6.
- [45] F. Richter, Y. Zhang, Y. Zhi, R. K. Orosco, and M. C. Yip, "Augmented reality predictive displays to help mitigate the effects of delayed telesurgery," in *Proc. Int. Conf. Robot. Autom.*, 2019, pp. 444–450.
- [46] X. Hou and S. Dey, "Motion prediction and pre-rendering at the edge to enable ultra-low latency mobile 6DoF experiences," *IEEE Open J. Commun. Soc.*, vol. 1, pp. 1674–1690, 2020.
- [47] M. Yang, C. Bian, and H.-S. Kim, "OFDM-guided deep joint source channel coding for wireless multipath fading channels," *IEEE Trans. Cogn. Commun. Netw.*, vol. 8, no. 2, pp. 584–599, 2022.
- [48] D. Molchanov, A. Ashukha, and D. Vetrov, "Variational dropout sparsifies deep neural networks," in *Proc. 34th Int. Conf. Mach. Learn.*, vol. 70, 2017, pp. 2498–2507.
- [49] P. Wu, X. Jia, L. Chen, J. Yan, H. Li, and Y. Qiao, "Trajectory-guided control prediction for end-to-end autonomous driving: A simple yet strong baseline," in *Proc. Adv. Neural Inf. Process. Syst.*, vol. 35, 2022, pp. 6119–6132.
- [50] K. Cho, B. van Merriënboer, C. Gulcehre, *et al.*, "Learning phrase representations using RNN encoder–decoder for statistical machine translation," in *Proc. Conf. Empirical Methods Nat. Lang. Process.*, 2014, pp. 1724–1734.
- [51] Z. Zhang, A. Liniger, D. Dai, F. Yu, and L. Van Gool, "End-to-end urban driving by imitating a reinforcement learning coach," in *Proc. Int. Conf. Comput. Vis.*, 2021, pp. 15 222–15 232.
- [52] F. Bellard. "BPG image format." (2014), [Online]. Available: <https://bellard.org/bpg/>.
- [53] Y. M. Saidutta, A. Abdi, and F. Fekri, "Joint source-channel coding over additive noise analog channels using mixture of variational autoencoders," *IEEE J. Sel. Areas Commun.*, vol. 39, no. 7, pp. 2000–2013, 2021.
- [54] 3rd Generation Partnership Project (3GPP), "5G; NR; Physical Channels and Modulation (3GPP TS 38.211 version 16.2.0 Release 16)," 3GPP, Tech. Rep., 2020, [Online]. Available: <https://www.3gpp.org>.